ROYAL SOCIETY
OF CHEMISTRY

EDGE ARTICLE

Check for updates

All publication charges for this article
have been paid for by the Royal Society
of Chemistry

pH-tunable membrane-active polymers, NCMNP2a-*x*, and their potential membrane protein applications†

Thi Kim Hoang Trinh, [ID] ‡[ab] Andres Jorge Cabezas,‡[cd] Soumil Joshi,‡[e]
Claudio Catalano,[ab] Abu Bakkar Siddique,[ab] Weihua Qiu,[ab] Sanket Deshmukh, [ID] [e]
Amedee des Georges [ID] [cdf] and Youzhong Guo [ID] *[ab]

Accurate 3D structures of membrane proteins are essential for comprehending their mechanisms of action and designing specific ligands to modulate their activities. However, these structures are still uncommon due to the involvement of detergents in the sample preparation. Recently, membrane-active polymers have emerged as an alternative to detergents, but their incompatibility with low pH and divalent cations has hindered their efficacy. Herein, we describe the design, synthesis, characterization, and application of a new class of pH-tunable membrane-active polymers, NCMNP2a-*x*. The results demonstrated that NCMNP2a-*x* could be used for high-resolution single-particle cryo-EM structural analysis of AcrB in various pH conditions and can effectively solubilize *Bc*TSPO with the function preserved. Molecular dynamic simulation is consistent with experimental data that shed great insights into the working mechanism of this class of polymers. These results demonstrated that NCMNP2a-*x* might have broad applications in membrane protein research.

Introduction

Membrane proteins are involved in numerous vital biological processes, such as chemotaxis in bacteria, photosynthesis in plants, vision, hearing, and heart rhythm in animals, as well as more complex cognitive processes in humans.[1,2] Due to their necessity, membrane proteins are also among the primary drug targets on the market.[3] Precise three-dimensional atomic structures are in high demand to comprehend the active mechanisms of membrane proteins. Before 2013, most membrane protein 3D structures were determined using X-ray crystallography; nevertheless, the recent resolution revolution in single-particle cryo-transmission electron microscopy (cryo-EM) has garnered tremendous attention. It can circumvent

significant limitations of crystallography, such as difficulties in obtaining diffracting membrane protein crystals. Cryo-EM is particularly useful for visualizing the conformation of a target protein in a frozen-hydrated state and requires only a minute amount of protein. Membrane proteins are typically extracted from the cell membrane using detergents for structural analysis. Unfortunately, these detergents can wreak havoc on the natural bilayers of cell membranes, resulting in instability, loss of function, and structural alterations of membrane proteins.[4] In cryo-EM studies, they can cause a decrease in water surface tension, which makes it challenging to control ice thickness and protein distribution in cryo-EM grids. Their micelles degrade the background of cryo-EM images.[5,6] Therefore, several modern methods (*e.g.*, liposome,[7] nanodiscs,[8] saposin-derived lipid nanoparticle,[9] and amphipol,[10] *etc.*) have been applied to reconstitute membrane protein into more stable single particles. Although these strategies improve the success of cryo-EM structural analysis, they necessitate an initial detergent solubilization step prior to reconstitution, which in some cases still faces the same challenges as previously described.

Recently, detergent-free techniques, such as styrene–maleic acid lipid particle (SMALP) and native cell membrane nano-particle (NCMN) systems, have emerged as promising alternatives to detergent-based techniques.[11,12] Membrane-active polymers, such as styrene–maleic acid (SMA) copolymers and derivatives, are the most important element of detergent-free systems. In an ideal situation, membrane-active polymers will

[a]Department of Medicinal Chemistry, School of Pharmacy, Virginia Commonwealth University, Richmond, VA 23298, USA. E-mail: yguo4@vcu.edu

[b]Institute for Structural Biology, Drug Discovery and Development, School of Pharmacy, Virginia Commonwealth University, Richmond, VA 23219, USA

[c]Structural Biology Initiative, CUNY Advanced Science Research Center, City University of New York, New York, New York, 10017, USA

[d]PhD Program in Biochemistry, The Graduate Center of the City University of New York, New York, New York, 10017, USA

[e]Department of Chemical Engineering, Virginia Tech, Blacksburg, VA2 4060, USA

[f]Department of Chemistry & Biochemistry, City College of New York, New York, New York, 10017, USA

‡ Co-first authors.

preserve the native macromolecular complex in nanoparticles, including membrane proteins in their native state and their native lipid bilayer belt surrounding the transmembrane domain. In this scenario, native protein–protein and protein–lipid interactions are preserved, and consequently, the membrane protein retains the same potential functionality as its counterpart on the cell membrane. SMA copolymers are the most prevalent membrane-active polymers capable of advancing structure determination by various techniques, such as solid-state NMR,[13] X-ray crystallography,[14] and cryo-EM.[6] However, they still have significant limitations. SMA copolymers are not always capable of preserving membrane proteins in their native state[15] and they are incompatible with divalent cations and low pH conditions.[16,17] Moreover, buffer conditions with a pH higher than 7 are necessary for the successful application of SMA copolymers, in which the carboxyl groups of polymer serve as the only water-soluble functional groups.[18]

Numerous efforts have been made to produce SMA derivatives and other alternative polymers to circumvent these constraints. Four broad strategies have been employed to date: (1) advances in synthetic methods,[19,20] (2) diversification of styrene: maleic acid ratio,[19,21] (3) modification of the hydrophobic domain, and (4) modification of the hydrophilic groups.[22,23] Efforts in substituting hydrophobic styrene units afford several novel backbones (e.g., stilbene–maleic acid,[24] diisobutylene–maleic acid,[25] and cycloalkane–maleic acid,[26] etc.). Changing the hydrophilic carboxylic groups is the most common way to improve pH and compatibility with divalent cations. Most attempts rely on the ring-opening of the inactive styrene–maleic anhydride (SMAnh) copolymer by primary amines. Thus, the carboxylic groups are replaced with other chemical groups. Various replacement head groups are available, including but not limited to alcohol,[27] amine,[22] or phosphobetaine[21] can alter the inherent properties of SMA in part or whole. Alternatively, the dehydration method that yields carboxylic-free polymers with positively charged maleimide subunits offers SMA-QA,[28] SMA-AA,[22] and SMI[29] exhibit excellent tolerance towards divalent cations at concentrations over 100 mM. However, they showed a peculiar/unusual pH behavior, where precipitation occurs out of pH 2.5–10 for SMA-QA, pH < 6 for SMA-AA, and pH < 7.8 for SMI. Variations in the intrinsic pK_a values of their positive head groups are the underlying cause of the differences. Although several disc-forming polymers have been developed, their use in biophysical characterization and high-resolution cryo-EM structure determination of membrane proteins has never been reported.

The primary objective of this research is to develop NCMN polymers compatible with a wide pH range and suitable for functional studies and high-resolution membrane protein structure determination. We have developed a new class of membrane-active polymers by ring-opening industrial SMAnh with a Brønsted base, tris(hydroxymethyl) aminomethane (Tris). These polymers are designated as NCMNP2a-x, where "x" represents the desired level of Tris grafting. We investigated the modified SMA to determine the effect of Tris content on applicability range (e.g., pH-active range and divalent cation resistance), membrane-active performance (e.g., solubilization

efficiency and NCMN particle characteristics), and the effect of neutral side groups on lipid selectivity. The applicability of these novel polymers was evaluated on two membrane protein model systems, the E. coli multidrug efflux pump AcrB and Bacillus cereus TSPO (BcTSPO). Depending on the level of Tris-grafting, the NCMNP2a-x are found to enhance their pH stability slightly or significantly, but they are still susceptible to Ca^{2+} concentrations of a few millimolar. We determined the high-resolution structure of AcrB and performed enzyme assays of functional BcTSPO under varying pH conditions to test the ability of these novel polymers to stabilize membrane proteins for functional and structural studies. To comprehend the working mechanism of membrane-active polymers, a coarse-grained (CG) molecular dynamics (MD) simulation was conducted to investigate the polymer–lipid bilayer interactions. Having proved that the MARTINI CG force field (FF)[30,31] is useful for SMA copolymers with styrene : maleic anhydride = 2 : 1,[32,33] it was applied in this study. We are convinced that NCMNP2a-x membrane-active polymers could serve as new substitutes for SMA copolymers and may be appropriate for functional and structural studies of various membrane proteins when pH conditions must be altered.

Results and discussion

Synthesis and characterization of NCMNP2a-x

Polymer synthesis. To overcome the limitations of SMA copolymers and to investigate possible influences of a reduction in carboxylic acid groups on polymer property and subsequent membrane protein solubilization, we developed a novel series of membrane-active SMA copolymers with partial diacid replacement. This new family of polymers was designated as NCMNP2a-x (x = 5, 25, 50, and 70, representing the desired Tris grafting percentages). NCMNP2a-x (x = 5, 25 and 50%) with low Tris incorporation were synthesized using Tris as a nucleophile to open SMAnh, followed by hydrolysis with NaOH (Fig. 1A). The absence of organic solvents and byproducts renders this procedure clean and environmentally friendly. While NCMNP2a-70, a polymer with a high Tris content, was prepared in two steps using DMF as the solvent (Fig. 1B). In this instance, every MAnh ring was opened with Tris which resulted in 50% of the target grafting, and the in situ Steglich amidation obtained the rest in the second step. The Steglich amidation was performed using Tris in the presence of TEA and $ClCO_2Et$. In this protocol, instead of yielding polymer chains of the singly grafted maleic acid unit, a mixture of polymer chains with doubly grafted maleic acid units formed. This heterogeneity results from the variable length and subunit sequence of commercially available SMAnh.

Structural characterization. ^{1}H-NMR spectroscopy was employed to characterize the polymer structure by observing the variations in chemical shifts (δ) (Fig. S1A†). The synthesis of NCMNP2a-x is based on the modification of hydrophilic MAnh, which does not affect the structure of styrene. Therefore, integral values of these aromatic protons could be used as a reference to determine the degree of Tris grafting on NCMNP2a-x. In the ESI,† detailed calculations and NMR spectra with complete
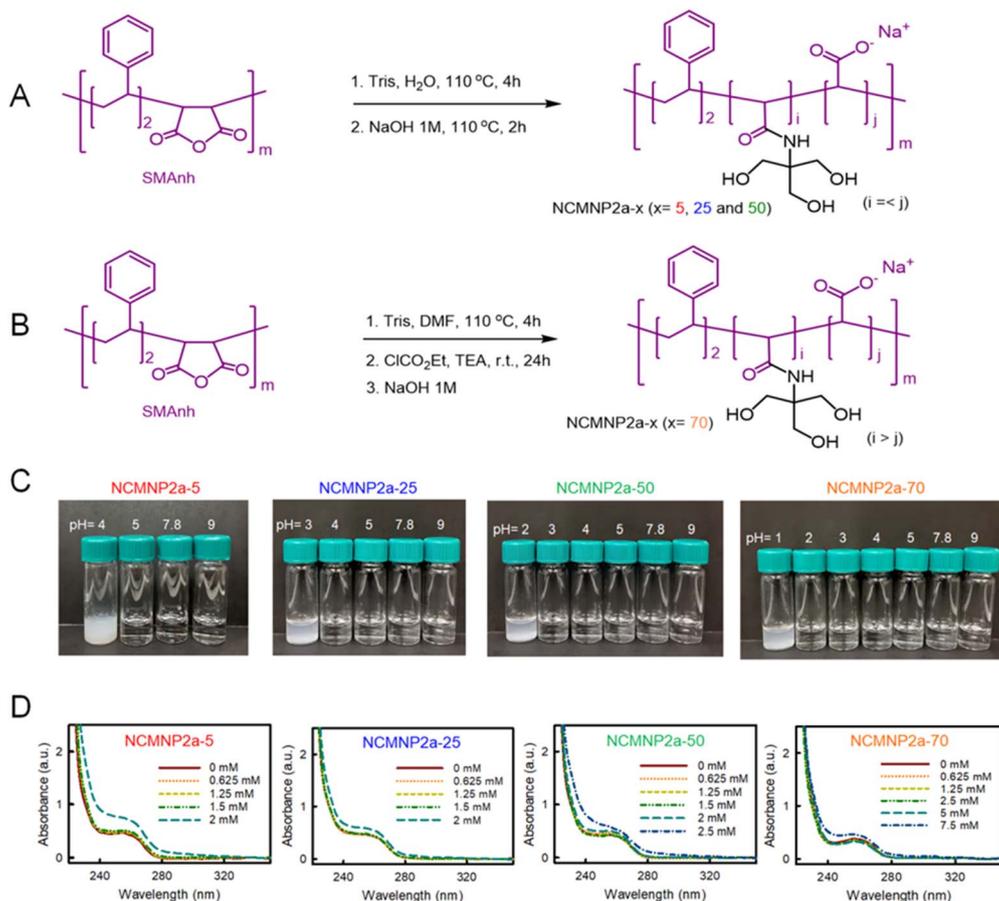
Fig. 1 Synthesis routine and physical characterizations of NCMNP2a-*x* polymers. (A) General schematic reaction for producing low Tris-grafting polymers (*x* = 5, 25 and 50). (B) General schematic reaction for producing high Tris-grafting polymer (*x* = 70). (C) Influence of Tris incorporation on the solubility of NCMNP2a-*x* (0.05% w/v) in the standard buffers containing 100 mM NaCl at various pH values. (D) A comparison of various NCMNP2a-*x* (0.05% w/v) in response to increasing quantities of divalent cation Ca^{2+}. Absorbance increase corresponds to polymer aggregates because of inter- and intermolecular binding of polymer chains to Ca^{2+}.

integration are presented (Section I and II, Fig. S2, S3, and Table S1†). The incorporation of Tris into the NCMNP2a-*x* backbone was determined to be 5.9%, 24.4%, 48.8%, and 65.7% for NCMNP2a-5, NCMNP2a-25, NCMNP2a-50, and NCMNP2a-70, respectively, *i.e.*, these results are consistent with the amounts of Tris used in their synthesis.

In support of the ¹H NMR characterization, a quantitative measurement has been performed to validate the grafting of Tris using FTIR (Fig. S1B and C†). The peak for vibrational C=O bond of amide obtained by the reaction of Tris with maleic anhydride and C=O bond of unreacted carboxylic acid were identified at 1645.1 cm⁻¹ and 1697.2 cm⁻¹. However, because of their proximity it was hard to quantify by normal analysis. To date several approaches has been explored such as absorbance, integral area and the occupied volume to quantify the functionality using FTIR data.[34–36] These days determination of peak integral area by deconvolution curve fitting has become popular because it offers detail qualitative and quantitative analysis of highly overlap or hidden absorbance peak which inspired the spectroscopic analysis of complex protein structure.[35,37,38] The spectra were deconvoluted considering two target Gaussian

center 1645.1 cm⁻¹ and 1697.2 cm⁻¹ for amide and carboxylic C=O bond. The deconvolution gives the occupied area of respective peaks. The grafting ratio was then calculated using this integrated area. We observed an incremental order for grafting functionalities as 24.46%, 50.33%, and 61.999% for NCMNP2a-25, NCMNP2a-50 and NCMNP2a-70 respectively which supports methods and ¹H NMR data analysis (Table S10†). However, the amide signal for NCMNP2a-5 inclined significantly and converged to the next broad peak which made it difficult to fit for functionality calculation.

pH and Ca^{2+} tolerance. Incompatibility with low pH and divalent cations are well-known limitations of SMA polymers. The neat SMA has a pK_{a1} of less than 6 and a pK_{a2} of less than 10, making it neutral, with a tendency to precipitate at acidic pH due to hydrophobic interactions.[23] Additionally, aggregation is caused by the electrostatic association of carboxylic acids with divalent cations. In the present work, however, the number of carboxylic acid groups has been partially replaced with amide groups and reduced relative to the parent SMA. This supports enhancing the solubility of NCMNP2a-*x*, as determined by turbidity experiments conducted at the concentration used in

functional and structural experiments (0.05% w/v). Through analysis, we illuminated the correlation between the Tris grafting degree and stability of NCMNP2a-x polymers (Table S1† and Fig. 1E and F). Desirably, substitutions of more carboxylic acid groups give the solubility of polymers at a broader pH range and higher [Ca^{2+}] tolerance. At pH = 5, while unmodified SMA begins to precipitate,[16] all modified polymers are entirely soluble. Among them, NCMNP2a-70, with the lowest acidic residue, remains soluble at the lowest pH condition (pH = 2). Additionally, it remains soluble in the presence of Ca^{2+} at concentrations up to 5 mM. Even though NCMNP2a-50 retains half of its carboxylic acid groups, it is still soluble at pH = 3. A similar result was previously reported with SMA-EA polymer, which has the same number of reduced carboxylic acids and uncharged hydroxyl head groups.[39] However, unlike SMA-EA, the stability of NCMNP2a-50 towards Ca^{2+} is not significantly improved, leading to aggregation at [Ca^{2+}] > 2 mM. The main reason is that pendant hydroxyl groups form a hydrogen bond with chloride ions and coordinate with calcium ions.[40,41] That results in a tightly packed network and eventually leads to aggregation. Generally, as proven in several studies,[42,43] strong calcium-binding occurs if carbohydrates can provide sites with at least three hydroxyl groups in a geometrical arrangement. Hence, SMA-EA that provides only a single hydroxyl group in each repeating unit is less sensitive to Ca^{2+} than NCMNP2a-50, which has three hydroxyl side groups. As a whole, our results suggest that the higher degrees of Tris grafting allow the polymers to tolerate much lower pH and a little higher [Ca^{2+}], thus significantly expanding the range of experimental conditions available to membrane protein solubilization.

Applications in membrane protein studies

The previous results demonstrate that their physical properties have improved. Consequently, this section examines whether our modified polymers can directly assemble NCMN particles from the native membrane for structural and functional studies.

AcrB solubilization and purifications. To answer this question, we chose an integral membrane protein AcrB, in *E. coli*,[44,45] as a model system for examining the solubilizing efficiency. Numerous variables, such as polymer concentration, ionic strength, and pH, may influence the solubilization of target proteins.[16,46] For instance, at a concentration of 2.5% w/v, SMA and its analogs perform the extraction of proteins from *E. coli* competently. However, as the concentration increases to 5% w/v, they become less effective.[21,25,47] It is believed that moderate salt concentrations (200–500 mM) promote membrane solubilization by decreasing electrostatic repulsion between the SMA and anionic lipids of the membrane.[46,48] Solubilization was tested at pH = 8.4 with the same final polymer concentration (2.5 percent w/v) and salt concentration (500 mM NaCl) (Fig. 2A). We selected a solubilizing pH of 8.4 because this is the optimal pH for SMA activity toward the cell membrane. At a slightly basic pH, the insertion of the hydrophobic styrene moiety into the lipid bilayer becomes more favorable, initiating the solubilization process.[49] Experimentally, upon the addition

of NCMNP2a-x polymers, the turbid cell membrane suspension spontaneously became transparent (except for NCMNP2a-70), providing a clear indication of the formation of the NCMN particles.

All NCMNP2a-x solubilized cell membrane samples were purified using the His-tag to eliminate other soluble fractions. The chromatograph of supernatants proceeded with the low Tris-grafting polymers, displaying single and sharp peaks at ~5 mL (Fig. 2B), demonstrating that the NCMN particles are present in eluent fractions. In contrast, no elution peak was observed after treatment with NCMNP2a-70, suggesting that no or very few NCMN particles were obtained. The collected peak fractions were additionally characterized by SDS-PAGE gel to detect contaminants, which revealed a single band with a molecular mass of approximately 110 kDa (Fig. 2C, lanes 1–3). This corresponds to the monomeric state of AcrB protein,[50] and demonstrates the success in the purification.

In contrast, the yields of NCMN particles decreased in inverse proportion to the number of reduced carboxylic acid groups on NCMNP2a-x side chains. NCMNP2a-5, which retained the most carboxylic acid side groups, produced the highest yield of NCMN particles, highly comparable to SMA2000 (Fig. S4A†), highlighting the significance of carboxylic acid in solubilization efficiency. Scheidelaar *et al.* proposed that membrane solubilization's "insight mechanism" for non-modified SMA[51] primarily occurs *via* the hydrophobic effect, wherein planar phenyl rings can insert between lipid acyl chains. Consequently, pendant carboxylic acid groups may also contribute to this effect. Due to their chemical nature, these acid groups can modulate the electrostatic interaction between polymer chains and lipid bilayers. The small size of the hydrophilic moieties provides a small cross-sectional area suitable for deeply penetrating the polymer into membranes, permitting the passage of solutes with a low molecular mass. Compared to SMA, NCMNP2a-x has uncharged and larger side groups, which eliminates electrostatic interaction and results in a larger cross-sectional area. Because of these chemical properties, the extraction efficiency of NCMNP2a-x is reduced.

We performed additional solubilization experiments with NCMNP2a-70 to confirm the formation of protein–lipid patches. Considering the presence of high molar mass fractions, the supernatant was collected using a centrifuge force of 64 000×g instead of 200 000×g as in previous tests. Predictably, A higher level of protein was obtained. The detectable chromatographic peak in the elution profile shifted to a lower retention volume than before. Our experience suggests that the cell membrane has been solubilized into larger NCMN particles that may not interact strongly with the Ni–NTA resin. (Fig. 2B and C (lane 4) and S4B†). The elution fraction displayed multiple bands on the SDS-PAGE gel, including the AcrB monomer. Therefore, it was assumed that these larger nanodiscs contained few AcrB molecules, with the majority of their mass coming from a significant contribution of surrounding lipids and other molecules with low molar mass.

Transmission electron microscopy. AcrB–NCMN particles resulting from NCMNP2a-5, NCMNP2a-25, and NCMNP2a-50 (5%, 25%, and 50% Tris-grafting polymers) exhibited
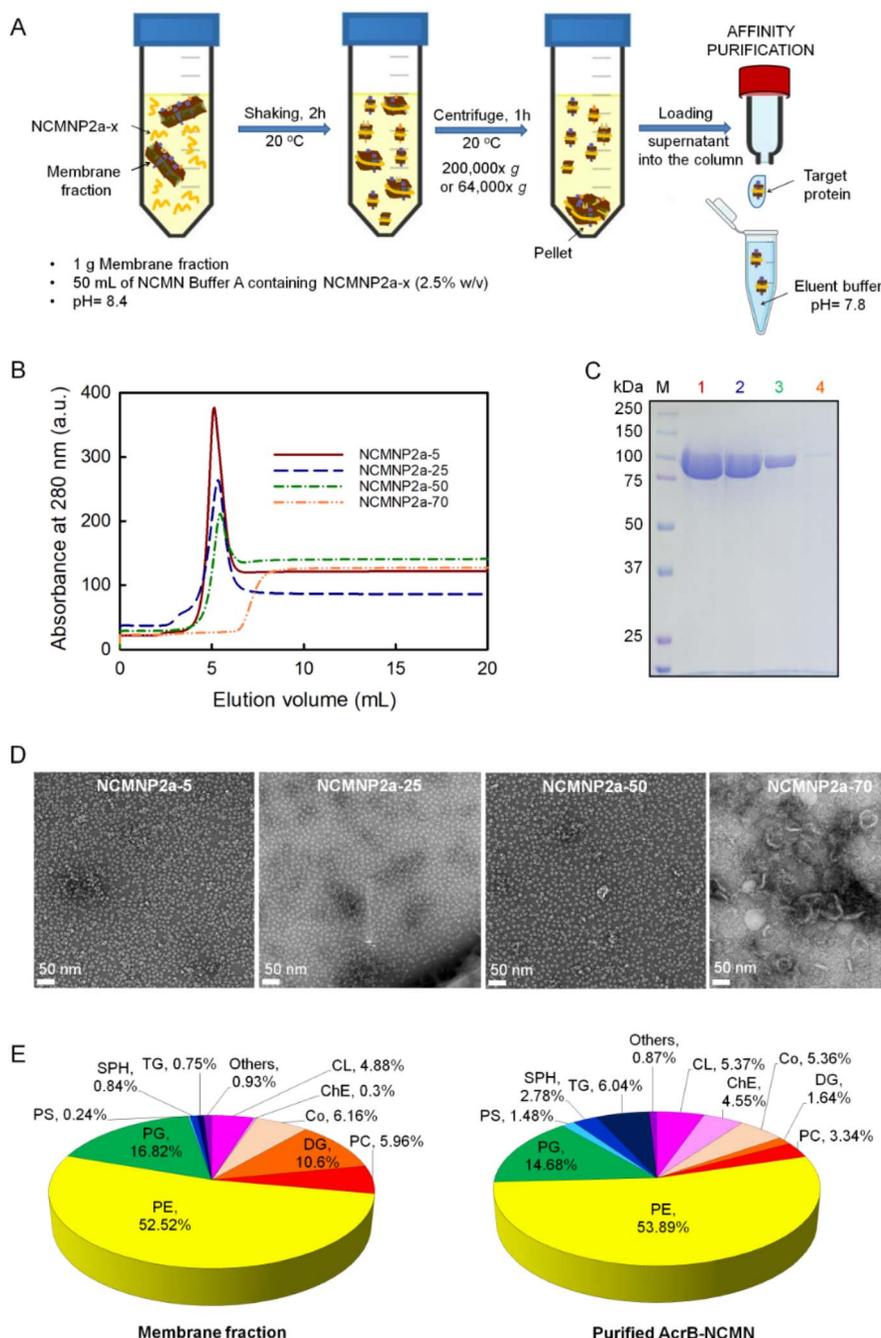
Fig. 2 Effect of Tris-grafting degree on membrane protein solubilization and size of AcrB−NCMN particles therefrom. (A) The typical procedure applied in the solubilization and purification of membrane proteins in this work. (B) Ni−NTA affinity chromatography profiles of purified AcrB in different NCMN polymers. (C) Analysis of AcrB−NCMN particles on SDS-PAGE along with protein marker (M). Lanes 1, 2, 3, and 4 correspond to purified AcrB extracted by NCMNP2a-5, NCMNP2a-25, NCMNP2a-50, and NCMNP2a-70, respectively. (D) Negative stain analysis of AcrB particles extracted by NCMNP2a-x polymers (x = 5, 25, 50, and 70). The bottom-left scale bar represents 50 nm. (E) Compositions of lipid species extracted from membrane fraction and purified AcrB determined by ESI-MS. Abbreviations included are cardiolipin (CL), cholesterol ester (ChE), coenzyme (Co), diglyceride (DG), phosphatidylcholines (PC), phosphatidylethanolamine (PE), phosphatidylglycerol (PG), phosphatidylserine (PS), sphingomyelin (SPH) and triglyceride (TG).

homogeneous and monodispersed particles with average diameters of 10 nm on negative stain EM micrographs (Fig. 2D). Notably, the triangular shape, a previously reported AcrB architecture,[52,53] was clearly maintained. In contrast, particles assembled themselves from NCMNP2a-70, where heterogeneity

and large encased lipid patches predominated. These observations support the above conclusion that a high number of Tris side chains causes NCMN particles to be larger. This is an intriguing property of NCMNP2a-70, as larger NCMN particles can retain more endogenous lipids than smaller NCMN

particles. Consequently, these constructs are appropriate for functional studies where complete conformational freedom and high lipid content are required to maintain activity.

In contrast, the smaller and more homogeneous AcrB–NCMN particles should be ideal for resolving 3D structures with high resolution using single-particle cryo-EM.

Lipid analysis. As is commonly known, SMALPs contain a lipid bilayer core surrounded by SMA. This buckling of polymer molecules induces a certain amount of lateral pressure on the lipid acyl chains, which can preserve the lipid packing from the natural environment. Therefore, the encapsulated membrane proteins retain the flexibility to allow conformational changes[54] and lipid–protein interactions[55,56] to regulate its essential function in some cases. These principal advantages make it possible to study the structure and function of membrane proteins in a membrane that closely resembles their native membrane. In addition, it has been demonstrated that SMA is not selective for any particular lipid, even in diverse cell membranes.[57,58]

However, the composition of the associated lipids in SMALPs differs from that of native membranes depending on membrane proteins and regions of cell membranes. As isolated by SMA, the major lipid components of *S. cerevisiae* mitochondria, where CytcO was expressed, did not change.[59] In contrast, Ayub *et al.* reported that CD81-SMALP isolated from *Drosophila* S2 appeared to be enriched in negatively charged lipids.[57] The disparity in lipid content is primarily the result of interactions between membrane proteins and lipids that surround them.[56] To identify potential lipid component alterations, we compared the extracted lipids of AcrB–NCMN particles derived from NCMNP2a-50 and the *E. coli* cell membrane. As depicted in Fig. 2E, the overall lipid profiles identified were comparably similar. Cholesterol ester (ChE), diglyceride (DG), and triglyceride (TG) concentrations exhibited the most notable variations (TG). We used a similar lipid extraction procedure,[58] but identified more lipid species instead of detecting only phosphatidylglycerol (PG). Phosphatidylethanolamine (PE), phosphoglycerol (PG), and cardiolipin (CL) were the major lipid components in both cases, which is consistent with the lipid components previously identified in the inner membrane of *E. coli* (55% PE, 15% PG, and 5% CL).[60,61] These promising findings suggest that our NCMN particles are capable of resolving the AcrB structure in a nearly native state.

High-resolution cryo-EM structure of AcrB–NCMN particles. Next, we examined whether the degree of Tris-grafting affected the ability of NCMN polymers to produce NCMN particles for single-particle cryo-EM structural determination. On Ultrafoil 1.2/1.3 grids, monodisperse AcrB particles extracted from NCMNP2a-5 and NCMNP2a-50 at varying pH were vitrified. Screening the grids showed uniform and monodisperse particles enabling us to collect high-resolution datasets (Table S2†). Two-dimensional (2D) class averages derived from the classification of achieving datasets showed clear features of a homotrimer with a triangular shape, similar to previous structures in SMA2000 and CyclAPols. (Fig. S5†).[26,62] The resulting 3D reconstructions have a final global resolution of 3.51, 3.05 and 3.07 Å for AcrB in NCMNP2a-5 (pH = 7.8), NCMNP2a-50 (pH =

7.8) and NCMNP2a-50 (pH = 5), respectively (Table S3†). The secondary structure and most side chains were well resolved at these resolutions, with clear EM densities that were highly comparable to previous AcrB structures in the liposome, SMA, and CyclAPols.[7,62,63] These findings suggest that our NCMN polymers are well suited for single-particle cryo-EM analysis.

None of our refined structures caused notable changes in the internal structure compared to the SMA2000-derived structure and each other (root-mean-square deviation values in a range of 0.425–0.897 Å, see Table S4†). The SMA2000 structure, however, lacked one-helix (Iα), whereas all 36 transmembrane helices (TMs) were identified in our three structures (Fig. 3A and S6†). It is tempting to hypothesize that, in comparison to SMA2000, those unique polymers better retain native lipids and, as a result, better stabilize the structure of the more flexible regions, like the outer-helix (Iα).[64] Despite varying Tris concentrations, all NCMN polymers retain endogenous lipids within the lipid cavity of AcrB (Fig. 3B). Liposomes and CyclAPols, on the other hand, could not achieve this.[7,63] In contrast to outcomes reported with detergent systems, the tight packing of these lipids in the inner leaflet can prevent the collapse of TM domains (Fig. S7†) and support efflux activity.[65] According to the aforementioned lipid analysis, it shows that the new hydroxyl groups may preserve native lipids as well as SMA2000, or even better, making them appropriate for cryo-EM research.

Three subunits comprise the asymmetric trimer-like AcrB structures, and each subunit has a unique conformation corresponding to one of the three substrate/proton transportation phases (L state, T state, and O state).[62] As previously documented, specific residues such as D407, D408, K940, N941, and T978 are important components of the proton-relay network that undergoes rearrangements triggered by D408 protonation/deprotonation.[66,67] Although this conformational change is a protonation-driven mechanism, no experiment has yet demonstrated the effect of solution pH on it. In this study, the enhanced pH resistance of NCMNP2a-50 enables us to investigate their potential structural change at pH = 5. However, the residue-level structural analysis revealed no conformational changes in the proposed proton transport mechanism (Fig. 3C–E). K940 continues to form stable salt bridges with either D407 or D408 in protomers L and T, and it transfers from D408 to T978 in protomer O. In the latter instance, K940 maintains its ionic connection with D407, which is sustained by the formation of new hydrogen bonds between K940 and T978, and N941. At such an acidic pH, the protonation of D407 and D408, whose pK_as are lower than 5 by at least one pH unit, is assumed to be challenging.[66,67] These are consistent with previous structures (2HRT,[68] 6BAJ[62]) and the computational work of Yue *et al.*,[66] where the significant pH-dependent shift relative to basic pH was only found at pH values less than 5.

BcTSPO solubilization and functional study. Since it catalyzes the conversion of protoporphyrin IX to bilindigin, *Bacillus cereus* TSPO (*Bc*TSPO) is used as a model protein (Fig. 4A).[69,70] Fig. 4B and C illustrate the comparison of *Bc*TSPO solubilization/purification of several types of solubilizing agents: conventional detergent (2% *n*-dodecyl-β-D-maltopyranoside, DDM) solubilizes the native cell membrane with
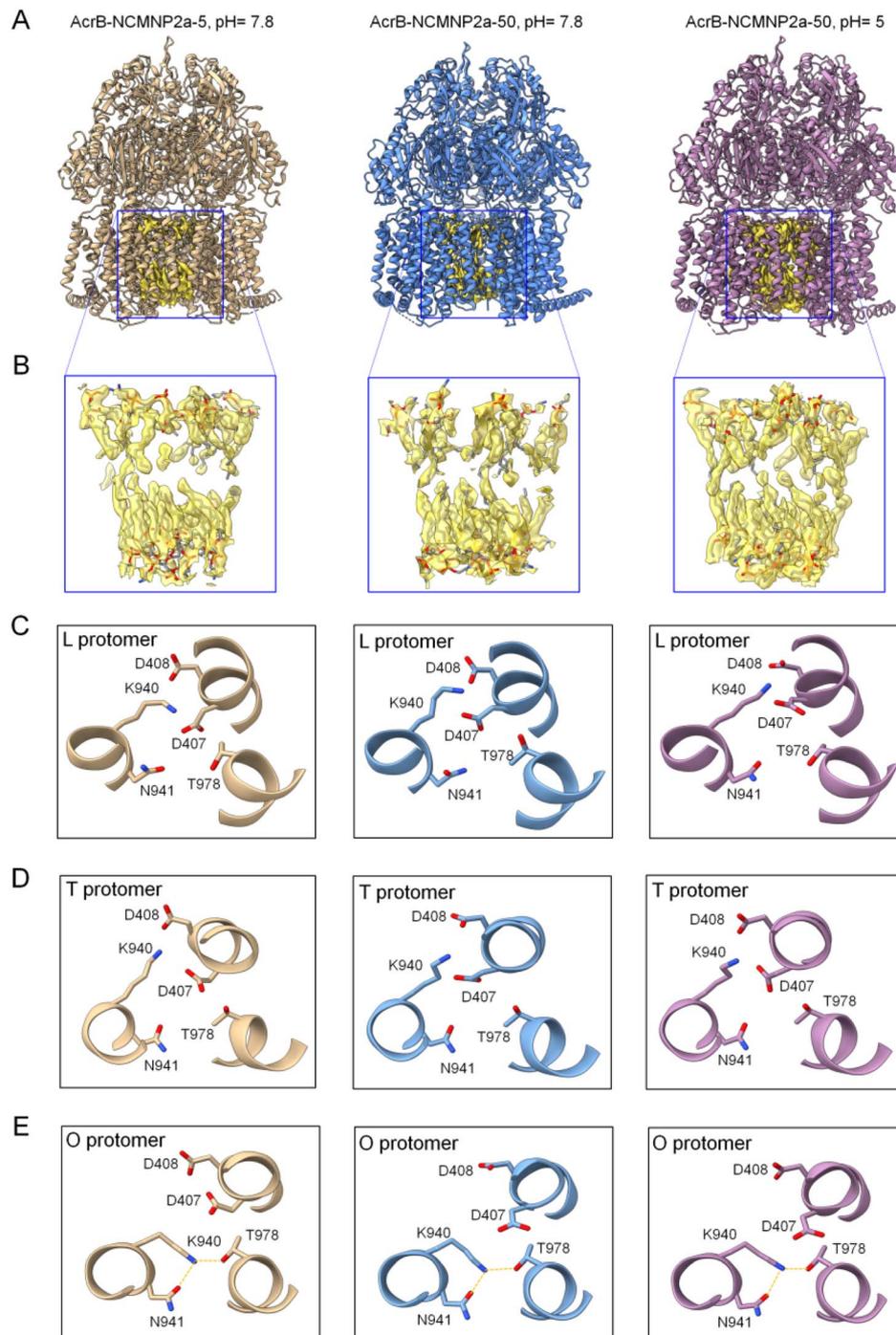
Fig. 3 Cryo-EM structures of AcrB−NCMN particles. (A) Ribbon diagrams of the entire AcrB complex warped by different polymers at various pH. These structures were obtained through manual fitting of the 6BAJ structure into the maps using Coot software. (B) Expanding views of blue box regions featuring the lipid bilayer located in the central cavity. The lipid bilayer was confidentially assigned with good quality of the EM map. (C) Configuration of protomer L of AcrB in different NCMN polymers. Left panel: NCMNP2a-5, pH = 7.8, middle panel: NCMNP2a-50, pH = 7.8 and right panel: NCMNP2a-50, pH = 5. (D) Configuration of protomer T of AcrB in different NCMN polymers. Left panel: NCMNP2a-5, pH = 7.8, middle panel: NCMNP2a-50, pH = 7.8 and right panel: NCMNP2a-50, pH = 5. (E) Configuration of protomer O of AcrB in different NCMN polymers with dotted lines (yellow) depicting the possible hydrogen bonds between residues. Left panel: NCMNP2a-5, pH = 7.8, middle panel: NCMNP2a-50, pH = 7.8 and right panel: NCMNP2a-50, pH = 5.

a relatively high efficiency (84.3%), which is significantly better than polymer solubilization. With polymer-based solubilization, SMA2000, a Tris-free polymer, and NCMNP2a-5 remove

membrane protein with greater efficacy than NCMNP2a-50 (Fig. 4C and S8†). These results are consistent with AcrB solubilization (see above). This demonstrates that the solubilization
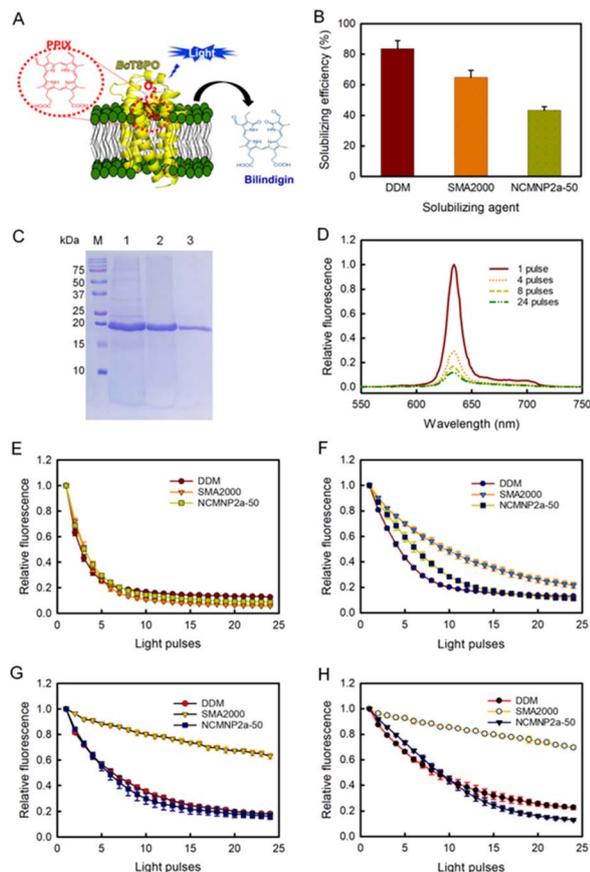
Fig. 4 Comparative effectiveness of differing solubilizing agents toward *Bc*TSPO solubilization and catalytic activity of corresponding *Bc*TSPO therefrom in the photodegradation of PpIX. (A) Schematic *Bc*TSPO induced photodegradation of PpIX into bilindigin. (B) Solubilization effectiveness of recombinant protein *Bc*TPSO in DDM, SMA2000 and NCMNP2a-50. (C) Visualization of purified *Bc*TSPO particles on Coomassie-stained SDS-PAGE compared to protein ladder (M). Lane 1, 2 and 3 correspond to *Bc*TSPO particles extracted by DDM, SMA2000 and NCMNP2a-50, respectively. (D) Representative fluorescent emission spectra of PpIX associated with *Bc*TSPO-NCMN particles upon excitation at 410 nm. (E)–(H) Photodegradation of PpIX in the presence of *Bc*TSPO at various pH conditions. Decays of PpIX at 632 nm as a function of the light pulse at pH = 7.8 (E). Decays of PpIX at 632 nm as a function of the light pulse at pH = 5 (F). Decays of PpIX at 632 nm as a function of the light pulse at pH = 4 (G). Decays of PpIX at 632 nm as a function of the light pulse at pH = 3 (H).

performance of polymers is inversely proportional to the amount of Tris on their side chains. In this study, in addition to NCMNP2a-5, NCMNP2a-50, which has a low sensitivity to acidic pH, was used to solubilize *Bc*TSPO to systematically investigate the potential impact of the levels of Tris grafting and different pH conditions on the functional performance of *Bc*TSPO in the following section.

For the enzyme activity assay, all investigations utilized an established methodology based on the fluorescence decay of PpIX.[71] In the absence of *Bc*TSPO, exposure of PpIX to light with a wavelength of 405 nm did not result in PpIX degradation (Fig. S9A†). Significant fluorescence degradation was seen when PpIX was exposed to 405 nm wavelength light in the presence of

*Bc*TSPO–NCMN particles (Fig. 4D). This indicates that *Bc*TSPO–NCMN particles have catalytic properties. At pH = 7.8, the intrinsic tryptophan fluorescence quenching profiles of *Bc*TSPO treated with NCMNP2a-5 and NCMNP2a-50 were remarkably similar to those of detergent-purified *Bc*TSPO and SMA2000-purified *Bc*TPSO samples (Fig. S10† and 4E). This demonstrates that even with additional functional side chains, there may only be a polymer–lipid interaction and no protein binding, keeping the protein intact and functional.[72,73] These findings indicate that *Bc*TSPO remained active, independent of the amount of Tris-grafting.

Next, we incubated *Bc*TSPO particles solubilized by DDM, SMA2000, and NCMNP2a-50 with PpIX at pH = 5, 4, and 3 to determine the effects of acidic pH on the degradation of PpIX catalyzed by *Bc*TSPO. All resulted in the degradation of PpIX upon excitation (Fig. 4F–H), with fluorescence decay rates depending on the individual *Bc*TSPO construct and the acidity of the reactive system. *Bc*TSPO particles derived from DDM and NCMNP2a-50 degrade at similar rates at the same pH settings but significantly more slowly than at pH = 7.8. In contrast, the activity of SMA2000-purified *Bc*TSPO is dramatically reduced at pH = 4 and pH = 3, while it is still effective at pH = 5. The latter observation may be related to the aggregation of *Bc*TPSO particles produced by a long-standing problem with SMA2000 belts, in which their carboxylic side groups undergo protonation at pH 5, resulting in electrostatic interaction between protein particles. Consequently, the creation of protein clusters likely hinders PpIX from associating with the active side of *Bc*TPSO.

At an acidic pH, the partial aggregation of PpIX (Fig. S9B†) and its protonation state reduce the catalytic activity.[74,75] Low pH could result in protonation of the propionic moiety on PpIX, a decrease in the solubility of PpIX in the reaction system, and a significant drop in its binding affinity to receptors. In conclusion, these results demonstrate the pH sensitivity of protoporphyrin IX breakdown by *Bc*TSPO. In addition, using NCMNP2a-50 with improved pH compatibility can circumvent the limitations of the present SMA2000 when speculating about the functional pH dependence of possible membrane proteins.

Coarse-grained molecular dynamics simulations. Coarse-grained (CG) molecular dynamics (MD) simulations were carried out using the MARTINI 3.0 force field to obtain a molecular-level understanding of the polymer interactions with lipids as well as their conformations.[30,31] As part of this study, we investigated the conformations of single polymer chains in water, the interactions between multiple polymer chains in water, and their self-assembly into NCMN nanoparticles (see more details in Section III in the ESI†). For simulations of individual polymer chains in water, it was observed that while all polymer chains collapsed in water due to their hydrophobicity, the variation in the percentage of charged COO^- groups as well as the steric effects of bulkier Tris groups significantly impacted the polymer conformations. Furthermore, the radial distribution functions (RDFs) between the entire polymer and water (Fig. 5A) indicated that as the percentage of Tris increased in the polymers, all peak heights reduced, resulting in a general dehydration of more Tris-
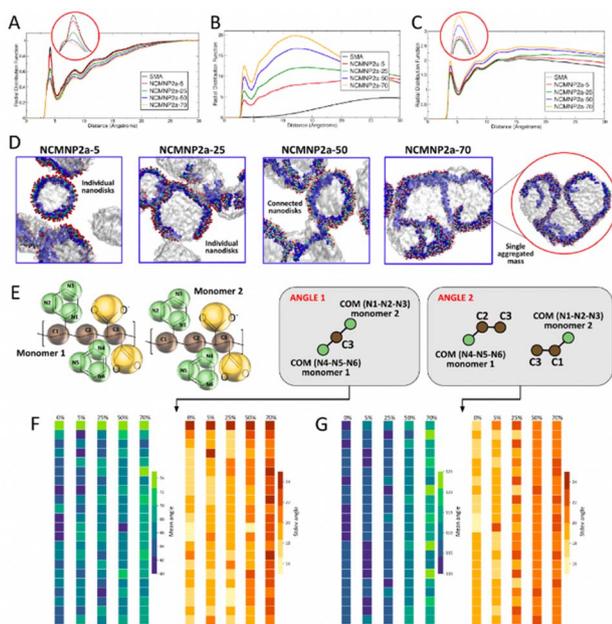
Fig. 5 Averaged RDF between (A) polymer–water (inset: zoomed-in first peak), (B) polymer–polymer, and (C) polymer–lipids (inset: zoomed-in first peak). (D) Simulation snapshots for all NCMNP2a-*x* systems studied. (E) Schematic showing the different angles calculated, (F) values for mean and standard deviations of angle 1 calculated for all monomers in the polymer chain, (G) values for mean and standard deviations of angle 2 calculated for all monomers in the polymer chain.

substituted polymers. In case of simulations containing six polymer chains dispersed in a box of water, it was observed that while all polymer chains still collapsed initially, polymer chains interacted strongly with each other when the Tris content was higher. This resulted in polymer aggregation and, thus, the higher structural correlation between polymer chains, in the case of NCMNP2a-50 and NCMNP2a-70 (Fig. 5B).

To understand the chemical basis of the experimentally observed behavior of nanoparticle formation, we performed CG MD simulations of the self-assembly of lipid–polymer nanoparticles. All simulations resulted in the formation of well-defined nanoparticles as shown in Fig. 5D, with the average diameters of most self-assembled nanoparticles between 8 and 10 nm, which agrees with our experimentally observed values as well as published literature.[32,33] At higher percentages of Tris substitution, nanoparticle interactions were found to be stronger with separate but connected nanoparticles observed in the case of NCMNP2a-50 and a solitary coalesced nanoparticle observed in the case of NCMNP2a-70. This was also reflected in the polymer–lipid RDFs (Fig. 5C) and was consistent with the experimentally observed behavior of high Tris-substituted polymer nanoparticles. To investigate the role of bulkier Tris groups in nanoparticle aggregation, we analyzed the angles formed by styrene and backbone beads across the maleic acid groups (Fig. 5E). As seen in Fig. 5F and G, The average values of the observed angles increased as the amount of Tris substitution increased. The standard deviation values also indicated

that these angles fluctuated more in the presence of increased Tris groups, providing the polymer chains greater conformational flexibility. Furthermore, calculating the solvent-accessible surface area (SASA) values for all styrene groups in the polymer chains showed an increase in styrene accessibility with an increase in Tris groups, which can be attributed to the conformational flexibility of these highly-substituted polymer chains. This increase in SASA, and thus, the accessibility of styrene, may result in increased lipid–polymer interactions in NCMNP2a-70, resulting in an aggregated mass opposite to individual nanoparticles in cases of lower Tris substitution.

Conclusions

We have designed, synthesized, and characterized a new class of membrane-active polymers, NCMNP2a-*x*. We demonstrated that this new class of polymers is suitable for high-resolution structure determination of the model membrane protein, AcrB, at different pH conditions. We also showed that NCMNP2a-*x* could be used to analyze the enzyme activity of *Bc*TSPO at different pH conditions. Variation of the grafting ratio of Tris on the SMA2000 backbone determines the pH sensitivity of the NCMNP2a-*x* polymers and also governs the cell membrane solubilization efficiency and subsequent size of NCMN particles. When solubilizing the cell membrane using NCMNP2a-70, very few AcrB–NCMN particles were obtained, and the size of such particles was much larger than that obtained using NCMNP2a-5 and NCMNP2a-50. Non-targeted membrane proteins were also encased as contaminants in such lipid bilayer patches. However, NCMNP2a-70 may be particularly useful when studying large membrane protein complexes. For example, these large and enriched cell membrane patches may be suitable for cryo-EM tomography analysis.

In contrast, the low Tris-grafted NCMNP2a-*x* polymers (≤50% of Tris) favored the solubilization of AcrB and its endogenous lipids into single particles suitable for single-particle cryo-EM analysis and can produce atomic-level membrane protein structures. Notably, Iα helix (TM) residues at the outer of helical bundles were fully resolved using NCMNP2a-*x*. In contrast, one of the Iα helix (TM) within the three subunits gave inferior EM density when using SMA2000. The lipid bilayer plugs were well preserved in all three cryo-EM structures at different pH conditions.

Molecular dynamic simulation analyses, including conformations of single polymer chains in water, interactions between multiple polymer chains in water and their self-organization into nanoparticles, and the formation of NCMN particles through polymer–lipid bilayer interaction, faithfully mimic the behaviors of various polymer systems as they are observed in experiments. This gives us a wealth of knowledge on the mechanics behind the interactions between polymers and lipid bilayers and paves the path for the future computer-aided rational design of membrane-active polymers that will enlarge the NCMN polymer library.

NCMNP2a-*x* are a new class of pH-tunable membrane-active polymers that retain native membrane protein function and are

suitable for high-resolution structure determination with single-particle cryo-EM. Therefore, they may have a wide range of applications in future membrane protein research.

Methods

Materials

Tris[hydroxymethyl]aminomethane (Tris), sodium dodecyl sulfate (SDS), ammonium persulfate (APS), 30% acrylamide/bisacrylamide solution, 37.5 : 1 (2.7% crosslinker), N,N,N',N'-tetramethylethylenediamine (TEMED) and tris(2-carboxyethyl)phosphine (TCEP) were purchased from Bio-Rad. On the other hand, 4-(2-hydroxyethyl)piperazine-1-ethanesulfonic acid (HEPES, ≥99%), glycerol (≥99.5%), nickel(II) sulfate hexahydrate (NiSO$_4$, >98%), imidazole (≥99%), hydrochloric acid (HCl, 36.5–38%), acetic acid (glacial, ≥99.7% w/w), methanol (MeOH, 99.8%), phenolphthalein (≥100% w/v), chloroform (≥99.8%, stabilized by ethanol) and sodium chloride (NaCl, ≥99%) with BioReagent or ACS grade were received from Fisher Chemical. DL-Dithiothreitol (DTT, ≥98% (HPLC), ≥99% (titration)), sodium hydroxide (pellets, ≥98%, reagent grade), sodium acetate (anhydrous, ≥99%, for molecular biology), protoporphyrin IX (≥95%) and triethylamine (TEA, ≥99%) were obtained from Sigma-Aldrich. n-Dodecyl-β-D-maltoside (DDM, Anagrade) was received from Anatrace. Ethyl chloroformate (ClO$_2$Et, 99%), deuterium oxide (D$_2$O, 99.9 atom% D), and N,N-dimethylformamide (DMF, anhydrous, 99.8%) were ordered from Acros that were stored in a dark brown glass bottle with a self-sealing septum. Poly(styrene-co-maleic anhydride) with a 2 : 1 ratio of styrene to MAnh (SMAnh, acid number: 355 mg KOH per g) were sold by Cray Valley. Before preparing different buffer solutions, water was double-deionized by a Millipore Milli-Q system to produce 18 MΩ deionized water (DI H$_2$O).

Synthesis of NCMN polymers

NCMNP2a-5, NCMNP2a-25, and NCMNP2a-50. Tris with a given amount (0.19 g, 0.96 g, and 1.92 g for NCMNP2a-5, NCMNP2a-25, and NCMNP2a-50, respectively) was well dissolved in 75 mL DI H$_2$O. Then, it was singly charged into a 250 mL flask containing SMAnh (5 g, 15.84 mmol of MAnh, 1 equiv.). Afterward, the mixture was heated under reflux at 110 °C for 4 h. NCMNP2a-50 clarified at this state while NCMNP2a-5 and NCMNP2a-25 were still turbid, indicating that a high amount of MAnh had remained unchanged. Therefore, these were further hydrolyzed with NaOH 1 M (25 mL) at 110 °C for 2 h until getting a transparent solution. All modified copolymers were cooled to room temperature and recovered by precipitating into HCl 12 N (pH < 2), before being washed 3 times in DI H$_2$O. The precipitates were next re-dissolved in NaOH 0.6 M and precipitated in HCl again. In the final step, the pH of each solution was adjusted to 7.8–8 and filtered through a 0.2 μm MilliporeSigma™ filter paper before lyophilization that afforded white powders in high yield (>97%).

NCMNP2a-70. There are two subsequent steps in the preparation of NCMNP2a-70. One is a simple ring-opening reaction of SMAnh using Tris as a nucleophile agent, and the other is an amide coupling reaction between carboxylic acid and amine. In the first step, to a round-bottom flask containing SMAnh (5 g, 15.84 mmol of MAnh, 1 equiv.) in 50 mL anhydrous DMF, Tris (2.015 g, 16.63 mmol, 1.05 equiv.) in 25 mL hot DMF was added and agitated at 110 °C for 4 h until obtaining a clear solution. In the second step, the yellow solution was cooled to 0 °C in an ice bath for 30 min, degassed, and placed under nitrogen before TEA (3.31 mL, 23.76 mmol, 1.5 equiv.) was added. The solution was agitated for 1 h following a dropwise addition of ClCO$_2$Et (2.26 mL, 23.76 mmol, 1.5 equiv.). After stirring for a further 1 h, Tris (0.84 g, 6.97 mmol, 0.44 equiv.) dissolved in 25 mL hot DMF was quickly added, and then the reaction mixture was continued agitating for 24 h at room temperature. Afterward, the polymer was purified through precipitation in 150 mL of cold acetone (twice). The white solid was collected and re-dissolved in 50 mL DI H$_2$O. In the final step, the pH of the solution was adjusted to 7.8–8 and filtered through a 0.2 μm MilliporeSigma™ filter paper before lyophilization that afforded white powder in high yield (>90%).

Structural characterization of NCMNP2a-x

Nuclear magnetic resonance (NMR) spectroscopy. All ^{1}H-NMR characterizations were performed on a Fourier 300 MHz with an incorporated autosampler. All samples were dissolved in D$_2$O except styrene–maleic anhydride in CDCl$_3$ solvent, and the spectra were recorded at room temperature.

Fourier-transform infrared spectroscopy (FT-IR). FTIR spectra were recorded on a Nicolet iS10 spectrometer (Thermo Scientific) equipped with a smart diamond ATR accessory. All absorbance spectra were collected from the gathering of 32 scans with a resolution of 4 cm^{-1} in the range of 4000–400 cm^{-1}. The deconvolution of the spectra were performed using OriginPro 2018 SR1 b9.5.1.195 (OriginLab Corporation), a software peak analyzer tool (baseline creation: analysis tool, peaks and baseline, peak analyzer, baseline creation, method 2nd derivative, number of 8 points to find, interpolation line method; baseline subtraction: analysis tool, data manipulation, subtract reference data; data fit: analysis, peaks and baseline, multiple peak fit, peak function Gaussian, number of peaks 10/11 in between wavenumber 800 cm^{-1} to 2000 cm^{-1} and rest of the information such as number of points, degrees of freedom and adj. R-square are given in the Table S10†).

Stability characterization of NCMNP2a-x

pH tolerance. pH sensitivity was determined by measuring the turbidity of polymers as a function of pH. Each NCMNP2a-x was diluted to a final concentration of 0.25% w/v in different buffers with pH in the range of 1 to 9. All buffer solutions contained 100 mM NaCl and Tris (pH 9), HEPES (pH 7.8), sodium acetate (pH 4–5), glycine (pH 2–3), or 12 N HCl (pH 0–1).

Calcium tolerance. Divalent cation sensitivity of each polymer was carried out as reported with the following modifications.[79] Calcium with various millimolar concentrations in HEPES buffer (50 mM HEPES, 100 mM NaCl, pH 7.8) was added separately into 0.1% w/v of corresponding NCMNP2a-x polymer.

The samples were vortexed vigorously and incubated at room temperature for 30 min.

Changes in absorbance in the range of 220–350 nm of all above samples were monitored by a NanoDrop™ 2000 spectrophotometer. Each of the experiments was repeated three times.

Expression, solubilization and purification of AcrB and *Bc*TSPO

The expression and cell lysis of AcrB and *Bc*TSPO membrane were carried out based on our previous protocol.[71,76] Following a typical solubilization procedure, 1 g membrane fraction was suspended in 10 mL NCMN Buffer A and then homogenized by using a Dounce homogenizer. Consequently, the suspended membrane was transferred to a 50 mL polypropylene tube and mixed with NCMNP2a-*x* for a final concentration of 2.5% w/v. After shaking the sample for 2 h at 20 °C, the insoluble species were centrifuged at 64 000×g (for NCMNP2a-70 media) and 200 000×g (for all other media) for 1 h 20 °C. The collected supernatant was loaded onto a 5 mL Ni–NTA column (GE Healthcare) pre-equilibrated with NCMN Buffer A at a flow rate of 0.5 ml ml^{-1}. Then, the column was washed with 30 mL of NCMN Buffer B and 30 mL of NCMN Buffer C before the protein was eluted with a mixture buffer of the NCMN Buffer C and NCMN Buffer D (1 : 1 v/v).

All the buffers were filtered with 0.22 μm MCE Membrane (MF-MilliporeTM) before use and their compositions are listed below:

- NCMN Buffer A: 50 mM HEPES, pH 8.4, 500 mM NaCl, 5% glycerol, 20 mM imidazole, 0.1 mM TCEP.

- NCMN Buffer B: 25 mM HEPES, pH 7.8, 500 mM NaCl, 40 mM imidazole, 0.1 mM TCEP.

- NCMN Buffer C: 25 mM HEPES, pH 7.8, 500 mM NaCl, 75 mM imidazole, 0.1 mM TCEP.

- NCMN Buffer D: 25 mM HEPES, pH 7.8, 500 mM NaCl, 500 mM imidazole, 0.1 mM TCEP.

AcrB–NCMN particles characterizations

Transmission electron microscopy (TEM). Carbon-coated copper grids (400 nm mesh) were glow-charged for 30 s before separately loading 3.5 μL of AcrB–NCMN particles with 0.1 mg mL^{-1} of protein concentration and left for 1 min to absorb fully. Then, the grid surface was rinsed 3 times with DI H$_2$O followed by staining twice with filtered 2% w/v uranyl acetate for 1 min. Filter papers were utilized to remove surplus liquid in each stage that was continued air-dry for at least 1 min. Images were taken by a Tecnai F20 UVA transmission electron microscope working at 120 kV. Each sample was imaged at 62 000× magnification on a 4k × 4k CCD camera.

Lipid extraction. Lipids from AcrB–NCMN particles were directly extracted by chloroform/MeOH at 4 °C, as previously described with some modification. In detail, to 0.5 mL of NCMN particles ([AcrB] = 1.5 mg mL^{-1}, 1 volume), 2 volumes of chloroform and 1 volume of MeOH were added and stirred for 1 h before adding one more volume of chloroform. Then, the solution was continuously stirred for a further 15 min followed

by the addition of 1 volume of DI H$_2$O. After centrifuging at 13 000×g for 10 min, the organic layer was rinsed three times with 2 volumes of cold DI H$_2$O. Afterward, the organic phase was characterized by electrospray ionization mass spectrometry (ESI-MS). Another lipid extraction was performed with a native cell membrane using a similar method to compare lipid composition.

Electrospray ionization mass spectrometry (ESI-MS). The lipids were separated by reverse-phase LC using a Thermo Scientific Accucore Vanquish C18+ 2.1 (i.d.) × 150 mm column with 1.5 μm particles. The UHPLC used a binary solvent system at a 0.26 mL min^{-1} flow rate with a column oven set to 55 °C. Before injection of the sample, the column was equilibrated for 2 min with a solvent mixture of 99% mobile phase A1 (CH$_3$CN/H$_2$O, 50/50, v/v, with 5 mM ammonium formate and 0.1% formic acid) and 1% mobile phase B1 (CH$_3$CHOHCH$_3$/CH$_3$CN/H$_2$O, 88/10/2, v/v/v, with 5 mM ammonium formate and 0.1% formic acid) and after the sample injection (typically 10 μL). The A1/B1 ratio was maintained at 99/1 for 1.0 min followed by a linear gradient to 35% B1 over 2.0 min, then a linear gradient to 60% B1 over 6 min followed by a linear gradient to 100% B1 over 11 min. At this step the run was held at 100% B1 for 5 min, followed by a 2.0 min gradient return to 99/1 (A1/B1). The column was re-equilibrated with 99/1 (A1/B1) for 2.0 min before the next run. Each sample was injected twice for analysis in both positive and negative modes. For the initial full scan MS (range 300 to 200 m/z), the resolution was set to 120 000 with a data-dependent MS2 triggered for any analyte reaching 3e^6 or above signal. Data-dependent MS2 was collected at 30 000 resolutions. Data were analyzed using Thermo Scientific's Lipid Search 4.2 software.

Cryo-EM grid preparation, data collection and model building. A 2 μL of purified AcrB (1 mg mL^{-1}) was added onto a pre-glow discharged Ultrafoil 0.6/1.0 grids, blotted for 3.5–4 s, and vitrified in liquid ethane by using FEI Vitrobot IV. Data were acquired using an FEI Titan Halo 80–300 transmission electron microscope at 300 kV equipped with a Gatan K3 Summit direction electron detector camera at New York Structural Biology Center. Images of AcrB in NCMNP2a-5 (pH = 7.8), NCMNP2a-50 (pH = 7.8), and NCMNP2a-50 (pH = 5) were gained in electron counting mode with a pixel size of 0.87, 0.88 and 0.846 Å, respectively. Particles were picked using WARP 1.0.9. The WARP written as goodparticles.star files were imported to cryoSPARC v.3.1. The 2D classification was done to separate good particles from false positives. A *de novo ab initio* model for each sample was then generated. Heterogeneous refinement using AcrB and decoy volumes was done to separate good particles from false positives further. The final particles and corresponding volume were subjected to Non-uniform refinement resulting in the final reconstruction of AcrB at 3.51, 3.05, and 3.07 Å for in NCMNP2a-5 (pH = 7.8), NCMNP2a-50 (pH = 7.8) and NCMNP2a-50 (pH = 5), respectively. In the next step, Chimera was utilized to fit the initial maps with our previous AcrB structure in SMA2000 (PDB 6BAJ).[62] Before manually fitting in Coot, these maps were sharpened within Phenix. The atom models were built accordingly and refined several rounds with Phenix before deposits.

Activity assay of *Bc*TSPO

Before performing the activity assays, different reaction solutions were prepared following the procedures below:

• PpIX stock solution was prepared as follows: adding 1 μL of saturated PpIX in DMSO to 199 μL of Buffer E (pH 7.8) and then taking 50 μL of this mixture and diluting 4× with Buffer E (pH 7.8).

• Buffer E contains 40 mM HEPES, 100 mM NaCl, 0.1 mM TCEP, and 0.05% w/v DDM. The pH value was adjusted to 7.8, 5, 4, or 3, depending on the target pH of the experiments. The solution was filtered with 0.22 μm MCE membrane before use.

The enzyme activity tests were conducted following our previous protocol with some modifications.[71] Typically, 100 μL of *Bc*TSPO ([*Bc*TSPO] ~ 1 mg ml^{-1}) was mixed with 129 μL of Buffer E (pH 7.8, pH 5, pH 4 or pH 3) and 1 μL of PpIX stock solution. This media was transferred into a 5 mm square quartz cuvette and then incubated in the dark for 5 min. The reaction was initiated by opening the shutters and exciting the mixture at 405 nm. The fluorescence emission was monitored from 550 to 750 nm.

All experiments were conducted on a Shimadzu RF-53301PC fluorescence spectrometer. The samples were illuminated at 405 nm with excitation bandwidth at 1.5 nm. On the other hand, the emission spectra were recorded with emission bandwidth at 3 nm.

Determination of repeating units

In general, SMAnh's chain end contains cumene because, as known, it was industrially synthesized *via* radical polymerization with dicumyl peroxide as a thermal initiator. Unfortunately, the methyl protons (H$_b$ and H$_i$) signals at $\delta = 1.25$–1.27 ppm, which could be used as reference peaks to characterize the structure of SMAnh, were disturbed by other signals. Therefore, we used other data such as molecular weight (approximately 3 kDa) and St : MAnh (2 : 1) of SMAnh to determine the repeating units, x, and m. By combining them, a set of the following equations is obtained:

Molecular weight:

$$M_n = M_{CH_3} + (M_{CH_2} + M_{CH} + M_{C_6H_5})x + M_{C_4H_2O_3}m + M_{C_6H_5} + 2M_{CH_3}$$

$$3000 = 15.03 + (14.03 + 13.02 + 77.10)x + 98.06m + 77.10 + 30.06$$

$$2877.81 = 104.15x + 98.06m \quad (1)$$

Relationship of repeating unit: $x = 2m$ (2)

From (1) and (2): $x = 18.6$ and $m = 9.3$

That gives $x = 18.6$ and $m = 9.3$, respectively. Secondly, to validate accuracy, we recheck the calculation by integrating chemical shifts in the ^{1}H-NMR spectrum of SMAnh. However, it is impossible due to an overlap of aromatic protons ($\delta = 5.8$–8.0 ppm) from St and protons from solvent ($\delta = 7.26$ ppm). Take note that, as ignoring –COOH protons, the SMA has the same number of aromatic and aliphatic protons as its mother, SMAnh. Besides, the chemical shift of D$_2$O solvent at $\delta = 4.79$ ppm does not perturb any signals of SMA. Thus, SMA was selected to testify the calculation instead of SMAnh. With $x = 18.6$, the total aromatic protons were set at 98 protons, including 93 protons from St in repeating units and 5 protons from cumene chain end. As a result, the total aliphatic protons observed were 81.02 protons ($3I_{H_b} + (2I_{H_c} + I_{H_d}) \times x + I_{H_e} \times y + I_{H_g} \times z + 6I_{H_i} = 81.02$). Given that relationship between y and z is $y + z = 16.2$. Because SMA is obtained from the hydrolysis of SMAnh, the m value, in this case, is equivalent to $y = z = (y + z)/2 = 8.1$, which is relatively lower than the initial calculation. However, when applying these new values ($x = 18.6$ and $m = 8.1$) to recalculate M_n, it was found that $M_n \sim 2900$ g mol^{-1} is highly comparable to SEC data documented by the provider. On the other hand, setting the number of aliphatic protons of SMAnh to 81.02 protons gives 100.21 protons in the range of 5.7–8.5 ppm. That probably combines 98 aromatic protons from SMAnh and ~2 protons solvent. These results are relevant and consistent. Thereby, $x = 18.6$ and $y + z = 16.2$ were used as references to estimate the number of protons of structures shown in Fig. S2† and the degree of carboxylic acid modified by Tris in a later section.

Determination of Tris grafting degree

The calculation for Tris grafting degree. The percentage of Tris incorporated into the SMA backbone was calculated following the formula below:

$$\text{Tris grafting percentage} = \frac{y_n}{y_n + z_n} \times 100 \quad (3)$$

where: y_n and z_n ($n = 1, 2, 3$ or 4) are repeating units calculated based on integrating chemical shifts in ^{1}H-NMR spectra (Fig. S1†). Due to proton exchange with deuterium oxide (D$_2$O) solvent, the NH and OH protons from amide and free hydroxyl groups, respectively, can be entirely ignored. During hydrophilic modification, the number of aromatic protons of NCMNP2a-x is consistent with its from SMA. Therefore, the x_n value ($x_n = 18.6$) and the relationship between y_n and z_n ($y_n + z_n = 16.2$) are determined based on the characterization of commercial SMAnh and its hydrolysis SMA by ^{1}H-NMR (see the determination of repeating units section). Therefore, y_n, z_n, and Tris grafting percentages for each synthesized polymer were determined in detail, shown below and summarized in Table S1.†

Repeating units:

$$x_n = 18.6 \quad (4)$$

$$y_n + z_n = 16.2 \quad (5)$$

Total integration of aliphatic protons:

$$3I_{H_b} + (2I_{H_c} + I_{H_d}) \times x_n + (I_{H_e} + 6I_{H_f}) \times y_n + I_{H_g} \times z_n + 6I_{H_i} = \sum \text{aliphatic protons}$$

$$3x_n + 7y_n + z_n = \sum \text{aliphatic protons} - 9 \quad (6)$$

From (3)–(6), we calculated the Tris degrees of NCMNP2a-x and data are summarized in Table S1.†

Molecular dynamic simulation

Models and methods. Here, we used the MARTINI 3.0 FF to model the different Tris-substituted NCMNP2a-*x* polymers following the mapping scheme shown in Fig. S11.† MARTINI 3, compared to its predecessor, has been shown to have improved interaction balance, a variety of mapping schemes with different degrees of coarse-graining as well as an improved water model independent from other beads.[77,78] Three separate residues were modeled, which formed the basic building blocks for our polymer systems. Of these, residue SMA represented the conventional monomer of the styrene–maleic acid polymer in $2:1$ ratio. Here, the COO^- group was modeled using the negatively charged SQ5n bead to appropriately mimic lower pH conditions. The residue SMT consisted of a single COO^- (SQ5n bead) replaced with the Tris group while the residue TRI consisted of both COO^- beads replaced with Tris groups. As COO^- groups were replaced with the larger Tris groups, the total charge on the residues decreased as these substituted groups could not dissociate in low pH conditions. Thus, these residues differed significantly in their bulkiness as well as total charge in lower pH conditions, replicating experimentally. Using different arrangements of these building residues, polymers with 0%, 5%, 25%, 50%, and 70% Tris substitution were generated, representing the experimentally studied NCMNP2a-*x* systems as shown in Fig. S12A.† Polymer chains were created with 23 repeating units to maintain coherence with the aforementioned CG MD studies on SMALP formation and are shown in Fig. S12B.‡[32,33]

In the case of the single and multi-polymer simulations, polymer chains representing NCMNP2a-*x* systems were randomly dispersed in a box of water along with neutralizing sodium ions and water beads. Polymer chains with varying initial configurations and arrangement of residues were simulated to incorporate a factor of disorder that may be observed in experiments. In order to study the self-assembly of lipids and polymers into nanoparticles, systems containing 6, 12, and 18 polymer chains were created with fixed numbers of lipids, randomly dispersed into a cubic box with size 25 nm × 25 nm × 25 nm, which was solvated with ∼40 000 water beads (∼164 000 all-atom water molecules). To appropriately reproduce the distribution of lipid components as observed in the experimentally isolated nanoparticles, we used PE (75%) and PG (25%) lipids in our CG MD simulations. Particularly, the smaller 1,2-dilauroyl-*sn*-glycero-3-phosphoethanolamine (DLPE) (580 molecules) and 1,2-dilauroyl-*sn*-glycero-3-phosphoglycerol (DLPG) (200 molecules) were utilized to facilitate faster self-assembly.[32] Sodium ions were added for system neutralization. A representative snapshot of the system can be found in Fig. S12C.† Furthermore, uncharged simulations were also carried out for all three cases mentioned below to ascertain the impact charged beads had on polymer conformations, interactions, and nanoparticle formation.

Table S5† provides detailed information regarding all the systems and simulation run times. Simulations were performed for over 2 μs at 310 K with the NPT ensemble using most of the hyperparameters defined in the aforementioned studies. The NAMD package was used for this purpose and the system was considered to be periodic in all directions.[79] A timestep of 20 fs was used with a cutoff of 12 Å and dielectric value of 15, consistent with the MARTINI 3.0 FF. Polymer chains were visualized using the VMD package and analyzed for their general conformations using Radius of Gyration (R_g) calculations as well as their structural correlations with other system components from Radial Distribution Functions (RDFs).[80] All analysis was carried out using CPPTRAJ and in-house TCL and Python scripts for the last 1 μs of the simulation after the systems were observed to have been equilibrated.[81]

Individual polymer chains in water. Given the replacement of charged COO^- groups with uncharged and bulkier groups in the NCMNP2a-*x* polymers, it was necessary to investigate the changes in polymer conformations in the absence of lipid molecules. It was observed that all polymer chains collapsed in water due to their general hydrophobicity, with the styrene groups forming a core. The charged hydrophilic groups, pointing outwards, towards the water, were in turn stabilized through their interaction with water as well as through the aggregation of sodium ions around the collapsed polymer chains. Counting the number of sodium beads around each polymer chain indicated that NCMNP2a-5 and NCMNP2a-25 polymers were just as surrounded with sodium as the completely charged SMA chains. However, as expected, as the Tris substitution reached 50%, this number reduced greatly followed by even more reduction for NCMNP2a-70 as shown in Table S6.† Furthermore, it was observed that up to 25% addition of Tris groups did not hamper the overall polymer conformation, where SMA, NCMNP2a-5, and NCMNP2a-25 displayed similar overall R_g values. However, as the percentage of Tris was increased from 0% to 70%, there was a slight increase in the R_g values from 10.67 Å to 11.40 Å, respectively, as shown in Table S7.† This could be attributed to the increase in the number of bulkier hydrophilic groups. In order to further investigate the contribution of charged beads on individual polymer conformations, R_g values for the entire uncharged polymers and their backbones were also calculated as shown in Table S7.† Here, while the overall R_g values for uncharged polymers were slightly smaller than those for their charged counterparts, the general trend of an increase in R_g with the increase in Tris substitution was found to hold true. However, the backbone R_g was found to be near constant for all uncharged polymer chains and lower than the values for charged low Tris-substituted polymer chains indicating that the presence of charges resulted in relatively expanded conformations in polymer chains.

Next, we analyzed the structure of the solvent around the different polymer chains by plotting several RDFs between polymer components and water. To identify the origin of this behavior, we further analyzed the RDFs between water and the important individual components of every polymer chain as presented in Fig. S8.† It was observed that, while all individual components of the polymer showed dehydration as the percentage of Tris in the polymers increased, the difference was particularly large for the dehydration of the backbone (TC1 beads). The TC1 beads attached to charged COO^- groups

showed significantly taller peaks when these beads were present in high numbers resulting in an ordered structure of water around them. However, as the percentage of Tris groups increased in polymer chains, the structure of water appeared considerably disordered, as a result of the steric effect from bulkier groups. The structure of water around all hydrophilic beads (*i.e.* SQ5n, P2, and TN4a) showed slight dehydration with an increase in Tris content but did not affect the overall ordering of the water beads. RDFs were also calculated between the uncharged polymer chain components and water and followed the same general trend as the charged systems hinting that the presence of charges did not affect the bead's structural correlation with water.

To study the effect of Tris groups on the accessibility of hydrophobic backbone and styrene beads, we investigated the solvent-accessible surface areas (SASA) for the TC1 and TC5 beads as shown in Table S8.† The SASA for these hydrophobic beads can be imagined as the direct result of polymer conformations attained to stabilize these chains in their respective simulations. It was observed that in the case of backbone TC1 beads, SASA decreased as the percentage of Tris increased. However, this trend was exactly the opposite for the styrene TC5 beads where SASA increased with Tris substitution. This is especially interesting as it indicates that attributing the changes in SASA values to the steric hindrance of bulkier groups may not be adequate. Having previously observed that the presence of charges hampered the polymer backbone conformations, we also studied the SASA for the uncharged polymer systems as shown in Table S8.† It was observed that the SASA values for backbone TC1 beads were significantly lower for polymer chains with under 50% Tris substitution, while the SASA values for 50% and 70% substituted polymers were comparable to their charged counterparts. This, in addition to the increased backbone R_g for lower substituted polymer chains indicated that when the number of charged groups in polymers was high, to reduce their repulsions and assist their stabilization through solvent and ionic interactions, the charged groups had to be directed outwards, inevitably making the backbone beads more accessible to the solvent. This is also supported by the observation that the RDFs between TC1 beads attached to maleic acid groups were much more hydrated as compared to the TC1 beads attached to styrene groups at low percentages of Tris substitution (Fig. S13†). As the Tris substitution increased, there were reduced repulsions within the polymer and most of the backbone beads formed a central hydrophobic core, decreasing their accessibility. This highlights the importance of electrostatic interactions on polymer stabilization. The increase in SASA for the styrene TC5 beads. However, remained the same in the case of charged or uncharged simulations indicating that this was most likely due to the steric effects of the larger substituted groups.

Multiple polymer chains in water. Following the investigation of polymer interactions with water, it was essential to study how polymer chains interacted with each other and how the percentage of Tris substitution affected their behavior. This was done by simulating six randomly dispersed polymer chains in the presence of water and neutralizing sodium ions. While all

the polymer chains still collapsed in the initial phase of the simulations, the collapsed polymers seemed to interact strongly with each other when the Tris content in the polymer was high. This resulted in the formation of aggregated polymer masses in case of NCMNP2a-50 and NCMNP2a-70, while the collapsed polymers largely stayed away from each other in case of SMA, NCMNP2a-5, and NCMNP2a-25. These inter-polymeric interactions, in a way, were found to stabilize polymer chains in the solvent preventing them from collapsing as they did individually. It was observed that while the differences in R_g values for single polymer chain systems were very minute, in the multi-polymer chain systems, the average R_g values were found to increase from 10.6 Å to 16.67 Å as the Tris substitution increased from 0% to 70% as shown in Table S7.† R_g analysis for the uncharged system trajectories also showed similar values and the same trend as in the case of charged systems indicating that the presence of charge did not influence this behavior to a great extent.

To probe this further, the polymer–polymer RDF was plotted as shown in Fig. 5B, along with the RDFs between all individual components in the system shown in Fig. S14.† Contrary to those between polymer chains and water, polymer–polymer RDFs showed the highest structural correlations as the Tris content in polymers increased. Furthermore, all polymer systems with Tris groups displayed a predominant peak at ~3 Å indicating some amount of polymer–polymer interactions. This peak was missing in the RDF for SMA polymer chains as they never interacted with each other. However, when the same RDFs for uncharged simulations were observed, there did appear a peak for the SMA polymer chains indicating that the absence of charge improved polymer–polymer interactions, albeit only in case of the otherwise entirely charged polymer. Similar trends, of greater structural correlation with increasing Tris substitution, were observed for individual polymer component RDFs including TC1–TC1 and TC5–TC5 indicating that polymer chains that instantaneously interacted with each other did so through their hydrophobic backbone and styrene groups. Of these, the structural correlation between styrene groups of interacting chains was found to be much more dominant where clear ordering was observed in these RDFs (Fig. S14B†). Other RDFs including SQ5n–SQ5n, P2–P2, and TN4a–TN4a also displayed the same trend as shown by the overall polymer–polymer RDFs. Thus, the new polymer chains developed and investigated in this study showed much stronger inter-polymeric interactions than the conventionally studied SMA polymers. These increased interactions between polymers at higher Tris substitutions are hypothesized to result in nanoparticle aggregation that was observed experimentally.

Self-assembly of lipid nanodiscs. Finally, we performed CG MD simulations of the self-assembly of lipid–polymer nanoparticles to ascertain the driving force, at the molecular level, behind the experimentally observed nanoparticle formation behaviour. Systems with six, twelve, and eighteen polymer chains, with multiple starting configurations, were studied to investigate the formation of nanoparticles and compare our results with the experimental observations. In the cases of SMA, NCMNP2a-5, and NCMNP2a-25 polymer systems, around four

nanoparticles were observed, each having a diameter close to 8 nm. As the percentage of Tris substitution increased to 50% (NCMNP2a-50), however, three connected nanoparticles were observed with an average diameter close to 9 nm. Also, while these nanoparticles interacted with other nanoparticles in the system, they did not entirely coalesce into a single mass as was the case with NCMNP2a-70. This system showed only a single, large nanoparticle encompassing all the polymer chains and lipid molecules in the system. This behavior, while consistent with the experimental observations, is interesting to look at pertaining to our larger goal of identifying polymer systems that could replace SMA in the future.

To identify the reasons for this particular behavior, we studied the RDFs between the polymer chains and lipid molecules as shown in Fig. 5C. Here, complementary to the differences in simulation trajectories, it was observed that the structural correlation between polymer chains and lipids molecules was quite similar for SMA, NCMNP2a-5, and NCMNP2a-25, all of which displayed similar numbers of nanoparticles in quantity and size. In the case of NCMNP2a-50 and NCMNP2a-70, the first RDF peaks were found to be higher than the previous systems with NCMNP2a-70 polymers having the highest structural correlation with lipid molecules indicating the highest interactions with lipids. The same was also observed for the uncharged simulations indicating that charge had little role to play in the aggregation of polymers and lipids with over 50% Tris substitution (Fig. S17†). Similar behavior was observed in most individual component analyses between polymer beads and lipid head, glycerol, and tail groups (Fig. S15 and S16†). While most of this appeared to be resulting from increased correlations of the Tris component beads with lipid groups, the RDF between styrene TC5 beads and lipid tails also showed a significant increase in first peak height for NCMNP2a-70 (Fig. S15B†). This indicated that polymer chains with higher Tris substitution possibly interact strongly with lipids, and other polymers as previously mentioned, resulting in the aggregation of multiple nanoparticles. A detailed analysis of simulation trajectories suggested that styrene groups from polymers initiate the formation of lipid nanoparticles by interacting with the hydrophobic tails of lipid molecules. Note, similar observations have been reported in previous studies.[10,11]

Next, to probe the effect of bulkier groups on the conformation of styrenes, if any, we studied the angles created by styrene and backbone beads, across the maleic acid groups. These were calculated for each monomeric unit, in the last 1 μs of the simulation trajectories. It was clearly observed that the mean angle formed between the two benzene rings constituting N1–N2–N3 and N4–N5–N6 beads increased from ~60° to ~70°. As also seen from the standard deviations for these angles, the angles fluctuated more in the presence of Tris groups, providing the polymer chains greater conformational flexibility. The mean angles formed by individual styrene rings with the backbone beads also showed similar trends, where systems with higher Tris groups showed angles about ~20–25° larger, also resulting from larger fluctuations in these angles. This suggests that the presence of bulkier Tris groups certainly affected the conformations of styrene groups resulting in higher polymer–lipid

interactions. Hence, to identify how these angles affected the accessibility of each benzene ring, we calculated the solvent-accessible surface area (SASA) values for these rings, as shown in Table S9.† In both, single polymer, and self-assembly simulations, it was found that the SASA increased for the systems containing 70% Tris substitution. However, this increase was tremendously more significant in the case of the benzene rings constituting N4–N5–N6 beads, in both charged and uncharged simulations. Furthermore, it was observed that as the Tris substitution increased, the benzenes comprising of N1–N2–N3 and N4–N5–N6 showcased similar SASA values as compared to SMA and NCMNP2a-5 polymer chains where this difference was as large as 70 Å^2.

Data availability

The datasets of EM maps are provided in ESI Tables S2 and S3.† The experimental structure coordinates can be downloaded from RCSB PDB and EM maps can be downloaded from EMDB.

Author contributions

Y. G. conceived the project. Y. G., W. Q., and T. K. H. T. designed the experiments. T. K. H. T. synthesized and analysed all the polymers and performed protein purifications, cryo-EM structure determinations, and enzyme assays. A. J. C. and A. G. collected and processed the cryo-EM data. S. J., S. D., and Y. G. designed the molecular dynamic experiment, S. J. performed the computational molecular dynamic analysis. C. C. participated in solving the cryo-EM structures of AcrB. A. B. S. performed quantitative FTIR analysis. W. Q. performed molecular cloning and initial optimization of AcrB–NCMN particles. T. K. H. T. and Y. G. drafted the manuscript. All authors contributed to the revision of the manuscript. Y. G. supervised the project.

Conflicts of interest

Y. G. and T. K. H. T. are inventors of NCMNP2a-*x* (patent pending).

Acknowledgements

scientific and technical assistance. The funders had no role in study design, data collection, analysis, decision to publish, or manuscript preparation. The content is solely the authors' responsibility and does not necessarily represent the National Institutes of Health or other funding organizations' official views.

References

1 G. H. Wadhams and J. P. Armitage, *Nat. Rev. Mol. Cell Biol.*, 2004, **5**, 1024–1037.

2 M. Farhadi, E. Razmara, M. Balali, Y. Hajabbas Farshchi and M. Falah, *J. Cell. Mol. Med.*, 2021, **25**, 5869–5883.

3 H. Stahlberg, D. Fotiadis, S. Scheuring, H. Rémigy, T. Braun, K. Mitsuoka, Y. Fujiyoshi and A. Engel, *FEBS Lett.*, 2001, **504**, 166–172.

4 Y. Guo, *Crystals*, 2020, **10**, 86.

5 H. E. Autzen, D. Julius and Y. Cheng, *Curr. Opin. Struct. Biol.*, 2019, **58**, 259–268.

6 K. S. Simon, N. L. Pollock and S. C. Lee, *Biochem. Soc. Trans.*, 2018, **46**, 1495–1504.

7 X. Yao, X. Fan and N. Yan, *Proc. Natl. Acad. Sci.*, 2020, **117**, 18497–18503.

8 W. Mi, Y. Li, S. H. Yoon, R. K. Ernst, T. Walz and M. Liao, *Nature*, 2017, **549**, 233–237.

9 J. Frauenfeld, R. Löving, J.-P. Armache, A. F. P. Sonnen, F. Guettou, P. Moberg, L. Zhu, C. Jegerschöld, A. Flayhan, J. A. G. Briggs, H. Garoff, C. Löw, Y. Cheng and P. Nordlund, *Nat. Methods*, 2016, **13**, 345–351.

10 M. Liao, E. Cao, D. Julius and Y. Cheng, *Nature*, 2013, **504**, 107–112.

11 C. J. Brown, C. Trieber and M. Overduin, *Curr. Opin. Struct. Biol.*, 2021, **69**, 70–77.

12 Y. Guo, *Biochem. Soc. Trans.*, 2021, **49**, 1361–1374.

13 J. Radoicic, S. H. Park and S. J. Opella, *Biophys. J.*, 2018, **115**, 22–25.

14 J. Broecker, B. T. Eger and O. P. Ernst, *Structure*, 2017, **25**, 384–392.

15 C. Catalano, D. Ben-Hail, W. Qiu, P. Blount, A. des Georges and Y. Guo, *Membranes*, 2021, **11**, 849.

16 S. C. Lee, T. J. Knowles, V. L. G. Postis, M. Jamshad, R. A. Parslow, Y.-p. Lin, A. Goldman, P. Sridhar, M. Overduin, S. P. Muench and T. R. Dafforn, *Nat. Protoc.*, 2016, **11**, 1149–1162.

17 L. Unger, A. Ronco-Campaña, P. Kitchen, R. M. Bill and A. J. Rothnie, *Biochem. Soc. Trans.*, 2021, **49**, 1349–1359.

18 J. M. Dörr, S. Scheidelaar, M. C. Koorengevel, J. J. Dominguez, M. Schäfer, C. A. van Walree and J. A. Killian, *Eur. Biophys. J.*, 2016, **45**, 3–21.

19 A. A. Smith, H. E. Autzen, T. Laursen, V. Wu, M. Yen, A. Hall, S. D. Hansen, Y. Cheng and T. Xu, *Biomacromolecules*, 2017, **18**, 3706–3713.

20 B. D. Harding, G. Dixit, K. M. Burridge, I. D. Sahu, C. Dabney-Smith, R. E. Edelmann, D. Konkolewicz and G. A. Lorigan, *Chem. Phys. Lipids*, 2019, **218**, 65–72.

21 M. C. Fiori, W. Zheng, E. Kamilar, G. Simiyu, G. A. Altenberg and H. Liang, *Sci. Rep.*, 2020, **10**, 9940.

22 T. Ravula, N. Z. Hardin, S. K. Ramadugu and A. Ramamoorthy, *Langmuir*, 2017, **33**, 10655–10662.

23 S. Lindhoud, V. Carvalho, J. W. Pronk and M.-E. Aubin-Tam, *Biomacromolecules*, 2016, **17**, 1516–1522.

24 M. Esmaili and M. Overduin, *Biochim. Biophys. Acta, Biomembr.*, 2018, **1860**, 257–263.

25 A. O. Oluwole, B. Danielczak, A. Meister, J. O. Babalola, C. Vargas and S. Keller, *Angew. Chem., Int. Ed.*, 2017, **56**, 1919–1924.

26 A. Marconnet, B. Michon, C. Le Bon, F. Giusti, C. Tribet and M. Zoonens, *Biomacromolecules*, 2020, **21**, 3459–3467.

27 A. F. Craig, E. E. Clark, I. D. Sahu, R. Zhang, N. D. Frantz, M. S. Al-Abdul-Wahid, C. Dabney-Smith, D. Konkolewicz and G. A. Lorigan, *Biochim. Biophys. Acta, Biomembr.*, 2016, **1858**, 2931–2939.

28 T. Ravula, N. Z. Hardin, S. K. Ramadugu, S. J. Cox and A. Ramamoorthy, *Angew. Chem., Int. Ed.*, 2018, **57**, 1342–1345.

29 S. C. L. Hall, C. Tognoloni, J. Charlton, É. C. Bragginton, A. J. Rothnie, P. Sridhar, M. Wheatley, T. J. Knowles, T. Arnold, K. J. Edler and T. R. Dafforn, *Nanoscale*, 2018, **10**, 10609–10619.

30 S. J. Marrink, H. J. Risselada, S. Yefimov, D. P. Tieleman and A. H. de Vries, *J. Phys. Chem. B*, 2007, **111**, 7812–7824.

31 X. Periole and S.-J. Marrink, in *Biomolecular Simulations: Methods and Protocols*, ed. L. Monticelli and E. Salonen, Humana Press, Totowa, NJ, 2013, pp. 533–565, DOI: **10.1007/978-1-62703-017-5_20**.

32 M. Xue, L. Cheng, I. Faustino, W. Guo and S. J. Marrink, *Biophys. J.*, 2018, **115**, 494–502.

33 P. S. Orekhov, M. E. Bozdaganyan, N. Voskoboynikova, A. Y. Mulkidjanian, H.-J. Steinhoff and K. V. Shaitan, *Langmuir*, 2019, **35**, 3748–3758.

34 M. Tazreiter, P. Christian, R. Schennach, T. Grießer and A. M. Coclite, *Anal. Methods*, 2017, **9**, 5266–5273.

35 P. Laurson, P. Raudsepp, H. Kaldmäe, A. Kikas and U. Mäeorg, *AIP Adv.*, 2020, **10**, 085214.

36 R. Mao, M. B. Huglin and T. P. Davis, *Eur. Polym. J.*, 1993, **29**, 475–481.

37 A. Sadat and I. J. Joye, *Appl. Sci.*, 2020, **10**, 5918.

38 A. Brangule and K. A. Gross, *IOP Conf. Ser.: Mater. Sci. Eng.*, 2015, **77**, 012027.

39 T. Ravula, S. K. Ramadugu, G. Di Mauro and A. Ramamoorthy, *Angew. Chem.*, 2017, **129**, 11624–11628.

40 W. J. Cook, U. Thewalt and C. E. Bugg, *Biochem. Biophys. Res. Commun.*, 1976, **68**, 143–148.

41 Y. Lu, G. Deng, F. Miao and Z. Li, *J. Inorg. Biochem.*, 2003, **96**, 487–492.

42 W. J. Cook and C. E. Bugg, *J. Am. Chem. Soc.*, 1973, **95**, 6442–6446.

43 S. J. Angyal, in *Carbohydrate Chemistry–VI*, ed. W. M. Doane, Butterworth-Heinemann, 1973, pp. 131–146.

44 K. Poole, *Curr. Opin. Microbiol.*, 2001, **4**, 500–508.

45 D. Ma, D. N. Cook, J. E. Hearst and H. Nikaido, *Trends Microbiol.*, 1994, **2**, 489–493.

46 S. Scheidelaar, M. C. Koorengevel, C. A. van Walree, J. J. Dominguez, J. M. Dörr and J. A. Killian, *Biophys. J.*, 2016, **111**, 1974–1986.

47 A. O. Oluwole, J. Klingler, B. Danielczak, J. O. Babalola, C. Vargas, G. Pabst and S. Keller, *Langmuir*, 2017, **33**, 14378–14388.

48 M. C. Fiori, Y. Jiang, G. A. Altenberg and H. Liang, *Sci. Rep.*, 2017, **7**, 7432.

49 A. H. Kopf, J. M. Dörr, M. C. Koorengevel, F. Antoniciello, H. Jahn and J. A. Killian, *Biochim. Biophys. Acta, Biomembr.*, 2020, **1862**, 183125.

50 V. Postis, S. Rawson, J. K. Mitchell, S. C. Lee, R. A. Parslow, T. R. Dafforn, S. A. Baldwin and S. P. Muench, *Biochim. Biophys. Acta, Biomembr.*, 2015, **1848**, 496–501.

51 S. Scheidelaar, M. C. Koorengevel, J. D. Pardo, J. D. Meeldijk, E. Breukink and J. A. Killian, *Biophys. J.*, 2015, **108**, 279–290.

52 S. Murakami, R. Nakashima, E. Yamashita and A. Yamaguchi, *Nature*, 2002, **419**, 587–593.

53 D. Du, Z. Wang, N. R. James, J. E. Voss, E. Klimont, T. Ohene-Agyei, H. Venter, W. Chiu and B. F. Luisi, *Nature*, 2014, **509**, 512–515.

54 M. Jamshad, V. Grimard, I. Idini, T. J. Knowles, M. R. Dowle, N. Schofield, P. Sridhar, Y. Lin, R. Finka, M. Wheatley, O. R. T. Thomas, R. E. Palmer, M. Overduin, C. Govaerts, J.-M. Ruysschaert, K. J. Edler and T. R. Dafforn, *Nano Res.*, 2015, **8**, 774–789.

55 J. M. Dörr, M. C. Koorengevel, M. Schäfer, A. V. Prokofyev, S. Scheidelaar, E. A. W. van der Cruijsen, T. R. Dafforn, M. Baldus and J. A. Killian, *Proc. Natl. Acad. Sci.*, 2014, **111**, 18607–18612.

56 A. C. K. Teo, S. C. Lee, N. L. Pollock, Z. Stroud, S. Hall, A. Thakker, A. R. Pitt, T. R. Dafforn, C. M. Spickett and D. I. Roper, *Sci. Rep.*, 2019, **9**, 1813.

57 H. Ayub, M. Clare, I. Milic, N. P. Chmel, H. Böning, A. Devitt, T. Krey, R. M. Bill and A. J. Rothnie, *Biochim. Biophys. Acta, Biomembr.*, 2020, **1862**, 183419.

58 S. J. Hesketh, D. P. Klebl, A. J. Higgins, M. Thomsen, I. B. Pickles, F. Sobott, A. Sivaprasadarao, V. L. G. Postis and S. P. Muench, *Biochim. Biophys. Acta, Biomembr.*, 2020, **1862**, 183192.

59 I. A. Smirnova, D. Sjöstrand, F. Li, M. Björck, J. Schäfer, H. Östbye, M. Högbom, C. von Ballmoos, G. C. Lander, P. Ädelroth and P. Brzezinski, *Biochim. Biophys. Acta, Biomembr.*, 2016, **1858**, 2984–2992.

60 I. Prabudiansyah, I. Kusters, A. Caforio and A. J. M. Driessen, *Biochim. Biophys. Acta, Biomembr.*, 2015, **1848**, 2050–2056.

61 C. R. Raetz, *Microbiol. Rev.*, 1978, **42**, 614–659.

62 W. Qiu, Z. Fu, G. G. Xu, R. A. Grassucci, Y. Zhang, J. Frank, W. A. Hendrickson and Y. Guo, *Proc. Natl. Acad. Sci.*, 2018, **115**, 12985–12990.

63 A. J. Higgins, A. J. Flynn, A. Marconnet, L. J. Musgrove, V. L. G. Postis, J. D. Lippiat, C.-w. Chung, T. Ceska, M. Zoonens, F. Sobott and S. P. Muench, *Commun. Biol.*, 2021, **4**, 1–9.

64 C. Catalano, D. Ben-Hail, W. Qiu, P. Blount, A. des Georges and Y. Guo, *Membranes*, 2021, **11**, 849, DOI: **10.3390/membranes11110849.**

65 E. W. Yu, J. R. Aires and H. Nikaido, *J. Bacteriol.*, 2003, **185**, 5657–5664.

66 Z. Yue, W. Chen, H. I. Zgurskaya and J. Shen, *J. Chem. Theory Comput.*, 2017, **13**, 6405–6414.

67 T. Yamane, S. Murakami and M. Ikeguchi, *Biochemistry*, 2013, **52**, 7648–7658.

68 M. A. Seeger, A. Schiefner, T. Eicher, F. Verrey, K. Diederichs and K. M. Pos, *Science*, 2006, **313**, 1295–1298.

69 Y. Guo, R. C. Kalathur, Q. Liu, B. Kloss, R. Bruni, C. Ginter, E. Kloppmann, B. Rost and W. A. Hendrickson, *Science*, 2015, **347**, 551–555.

70 C. Ginter, I. Kiburu and O. Boudker, *Biochemistry*, 2013, **52**, 3609–3611.

71 Y. Guo, R. C. Kalathur, Q. Liu, B. Kloss, R. Bruni, C. Ginter, E. Kloppmann, B. Rost and W. A. Hendrickson, *Science*, 2015, **347**, 551–555.

72 S. Gulati, M. Jamshad, T. J. Knowles, K. A. Morrison, R. Downing, N. Cant, R. Collins, J. B. Koenderink, R. C. Ford, M. Overduin, I. D. Kerr, T. R. Dafforn and A. J. Rothnie, *Biochem. J.*, 2014, **461**, 269–278.

73 D. J. K. Swainsbury, S. Scheidelaar, R. van Grondelle, J. A. Killian and M. R. Jones, *Angew. Chem.*, 2014, **126**, 11997–12001.

74 D. Maitra, B. M. Pinsky, A. Soherawardy, H. Zheng, R. Banerjee and M. B. Omary, *bioRxiv*, 2021, preprint, DOI: **10.1101/2021.01.11.426224**.

75 L. M. Scolaro, M. Castriciano, A. Romeo, S. Patanè, E. Cefalì and M. Allegrini, *J. Phys. Chem. B*, 2002, **106**, 2453–2459.

76 K. G. Kroeck, W. Qiu, C. Catalano, T. K. H. Trinh and Y. Guo, *JoVE*, 2020, e61298, DOI: **10.3791/61298**.

77 P. C. T. Souza, R. Alessandri, J. Barnoud, S. Thallmair, I. Faustino, F. Grünewald, I. Patmanidis, H. Abdizadeh, B. M. H. Bruininks, T. A. Wassenaar, P. C. Kroon, J. Melcr, V. Nieto, V. Corradi, H. M. Khan, J. Domański, M. Javanainen, H. Martinez-Seara, N. Reuter, R. B. Best, I. Vattulainen, L. Monticelli, X. Periole, D. P. Tieleman, A. H. de Vries and S. J. Marrink, *Nat. Methods*, 2021, **18**, 382–388.

78 R. Alessandri, J. Barnoud, A. S. Gertsen, I. Patmanidis, A. H. de Vries, P. C. T. Souza and S. J. Marrink, *Adv. Theory Simul.*, 2022, **5**, 2100391.

79 J. C. Phillips, D. J. Hardy, J. D. C. Maia, J. E. Stone, J. V. Ribeiro, R. C. Bernardi, R. Buch, G. Fiorin, J. Hénin, W. Jiang, R. McGreevy, M. C. R. Melo, B. K. Radak, R. D. Skeel, A. Singharoy, Y. Wang, B. Roux, A. Aksimentiev, Z. Luthey-Schulten, L. V. Kalé, K. Schulten, C. Chipot and E. Tajkhorshid, *J. Chem. Phys.*, 2020, **153**, 044130.

80 W. Humphrey, A. Dalke and K. Schulten, *J. Mol. Graphics*, 1996, **14**, 33–38.

81 D. R. Roe and T. E. Cheatham III, *J. Chem. Theory Comput.*, 2013, **9**, 3084–3095.